RSC Advances

PAPER

View Article Online
View Journal | View Issue

Cite this: *RSC Adv.*, 2026, **16**, 13540

Platinum-supported catalysts on modified γ-Al_2O_3 carriers for enhanced NO oxidation in diesel exhaust aftertreatment

Xin Dai, [a] Jingfang Zhu,*[a] Dezhi Ren,[a] Fei Yu,[a] Shiying Chang*[ab] and Yunkun Zhao[a]

This study investigates the catalytic performance of platinum (Pt)-supported catalysts for nitric oxide (NO) oxidation in diesel vehicle exhaust aftertreatment systems, focusing on the effect of carrier modification. Pt catalysts were supported on γ-Al_2O_3, Ce-doped γ-Al_2O_3 (Ce-Al_2O_3), and La-doped γ-Al_2O_3 (La-Al_2O_3) *via* an excess impregnation method. Their physicochemical properties were characterized using inductively coupled plasma optical emission spectroscopy (ICP-OES), X-ray diffraction (XRD), transmission electron microscopy (TEM), CO pulse chemisorption, and X-ray photoelectron spectroscopy (XPS). Catalytic activity for NO oxidation was evaluated under simulated diesel exhaust conditions, and the reaction mechanism was probed by *in situ* diffuse reflectance infrared Fourier transform spectroscopy (*in situ* DRIFTS) and NO temperature-programmed desorption (NO-TPD). The results show that La- and Ce-modified Pt catalysts (especially Pt/LaAl) exhibit superior aging resistance and NO oxidation activity compared to unmodified Pt/Al_2O_3. For fresh catalysts, Pt/LaAl-f achieves a Pt dispersion of 50.48% (*vs.* 24.72% for Pt/Al-f) and an average Pt particle size of 5.75 nm (*vs.* 6.64 nm for Pt/Al-f). After aging at 750 °C for 10 h, Pt/LaAl-a retains a specific surface area of 94.31 $m^2\ g^{-1}$ (a 6.3% loss *vs.* 22.5% for Pt/Al-a) and a NO_2 proportion in NO_x of 42.1 ± 0.5% (*vs.* 28.3 ± 0.4% for Pt/Al-a). The enhanced performance of Pt/LaAl is attributed to the formation of $Al_{11}La_3$ intermetallic compounds, which provide additional NO adsorption sites and promote the generation of active intermediate species (*e.g.*, bridging/chelating nitrates). *In situ* DRIFTS confirms abundant adsorbed nitrate/nitrite species on Pt/LaAl, while NO-TPD shows its NO adsorption capacity (89.6 μmol g^{-1}) is nearly twice that of Pt/Al (45.1 μmol g^{-1}). This work provides critical insights for designing high-efficiency NO_x purification catalysts for diesel exhaust and industrial waste gas treatment.

Received 4th January 2026
Accepted 28th February 2026

DOI: 10.1039/d6ra00070c

rsc.li/rsc-advances

Introduction

Diesel engines are indispensable for modern transportation and industrial power generation due to their high thermal efficiency (>40%) and long-term reliability. However, their combustion process emits a complex mixture of pollutants, including nitrogen oxides (NO_x), particulate matter (PM), carbon monoxide (CO), and unburned hydrocarbons (HC).[1] These emissions pose severe threats to human health (*e.g.*, respiratory diseases) and the environment (*e.g.*, acid rain, smog formation). To address this, stringent emission regulations (*e.g.*, Euro VI, China VI) have been implemented globally, driving the development of advanced diesel exhaust aftertreatment systems.[2]

A typical diesel aftertreatment system consists of a diesel oxidation catalyst (DOC), a diesel particulate filter (DPF), and a selective catalytic reduction (SCR) system. The DOC plays a pivotal role: it oxidizes CO and HC to harmless CO_2 and H_2O, and converts NO to NO_2— a key step for downstream processes.[3] NO_2 enables passive regeneration of DPF by oxidizing PM at 250–350 °C (lower than the 500 °C required for active regeneration), reducing fuel consumption.[4] Additionally, a high NO_2/NO ratio (>1) enhances SCR efficiency, as SCR catalysts (*e.g.*, Cu-SSZ-13) preferentially reduce NO_2 with urea to N_2 (ref. 5).

Despite its importance, NO oxidation in DOC faces two major challenges: (1) competitive adsorption: CO and HC (incomplete combustion products) compete with NO for active sites on the catalyst surface, lowering NO oxidation efficiency;[6] (2) thermal deactivation: precious metals like Pt (the most active component for NO oxidation) tend to aggregate at high exhaust temperatures (400–700 °C), reducing the number of active sites.[7] To mitigate these issues, researchers have explored strategies such as optimizing catalyst carriers or introducing co-catalysts.

Traditional γ-Al_2O_3 is widely used as a DOC carrier due to its high specific surface area and good thermal stability, but it fails to suppress Pt aggregation under harsh conditions.[8] Emerging materials like metal–organic frameworks (MOFs) and covalent

[a]*Kunming Sino-Platinum Metals Catalyst Co.Ltd, Kunming 650106, China. E-mail: jingfang.zhu@spmcatalyst.com; shiying.chang@spmcatalyst.com*
[b]*State Key Laboratory of Precious Metal Functional Materials, Kunming 650106, China*

organic frameworks (COFs) offer high adsorption capacity, but their structural collapse at >500 °C limits industrial application. In contrast, doping γ-Al_2O_3 with rare earth elements (*e.g.*, La, Ce) has emerged as a cost-effective solution: La stabilizes the carrier's pore structure and maintains a high specific surface area, while Ce promotes oxygen storage/release *via* Ce^{3+}/Ce^{4+} redox cycles.[9,10] Previous studies have shown that La-doped Al_2O_3-supported Pt catalysts exhibit lower activation energy for NO oxidation than undoped ones[15], but the mechanism of La-enhanced activity and aging resistance remains unclear.

This work focuses on Pt catalysts supported on γ-Al_2O_3, Ce-Al_2O_3, and La-Al_2O_3. We systematically compare their physicochemical properties (Pt loading, dispersion, particle size) and NO oxidation activity (fresh and aged). The role of La/Ce in regulating carrier-Pt interactions, NO adsorption, and intermediate species formation is clarified *via in situ* characterization. Our goal is to identify the key factor governing NO oxidation activity and provide guidelines for designing durable DOC catalysts.

Experiment

Preparation of catalysts

This study utilized an excess impregnation method for catalyst preparation. The process comprised stirring the selected carrier with a specific volume of water to form a suspension, followed by incorporating a Pt precursor solution into the carrier suspension to achieve a 1 wt% Pt/carrier mixture. The mixture was subjected to magnetic stirring at room temperature for 3 hours, subsequently followed by a 2 hours static period. The recovered catalyst was subsequently dried at 120 °C for 12 hours. The resulting powder was subsequently calcined in a muffle furnace at 600 °C for 3 hours to yield the fresh catalysts, designated as Pt/Al-f, Pt/CeAl-f, and Pt/LaAl-f. The aged catalysts were fabricated by calcining the fresh catalysts in a muffle furnace at 750 °C for 10 hours, designated as Pt/Al-a, Pt/CeAl-a, and Pt/LaAl-a. The carriers utilized in this study for supporting noble metals were commercial γ-Al_2O_3, Ce-Al_2O_3, and La-Al_2O_3. The γ-Al_2O_3 was procured from Sasol, featuring a specific surface area of 120 m^2 g^{-1}, whereas the Ce-Al_2O_3 and La-Al_2O_3 were obtained from SOLVAY, with specific surface areas of 90 m^2 g^{-1} and 110 m^2 g^{-1}, respectively. The Pt precursor, *trans*-$[Pt(NH_3)4(OH)_2](CH_3COO)_2$, was supplied by Sino-Platinum Metals Co., Ltd.

Catalyst characterization

Platinum content was assessed using inductively coupled plasma optical emission spectroscopy (ICP-OES). X-ray diffraction (XRD) phase structure analysis was conducted on an X'Pert Pro powder X-ray diffractometer, employing a Cu Kα radiation source ($\lambda = 1.5406$ Å), a scanning speed of 10° min^{-1}, a scanning range of 2θ from 10° to 90°, and a step size of 0.02°. Transmission electron microscopy (TEM) images were acquired using a JEM 2100 operating at an acceleration voltage of 200 kV. The average size of Pt nanoparticles was determined by counting 200 particles from TEM images. The CO pulse adsorption experiments were carried out on a Chem BET 3000 analyzer. A 100 mg catalyst sample was introduced into a U-shaped quartz tube, with a small amount of quartz wool positioned at the outlet. After preprocessing, high-purity CO (99.9%) was given 10 consecutive pulses, and the gas signal was recorded by TCD. The dispersion calculation is based on the following formula:

$$V_{CO} = \sum \frac{(A_c - A_i)}{A_c} V_c \times \frac{273}{(273 + T)} \times \frac{P}{760}$$

In the formula, A_c is the average peak of the total amount of unabsorbed gas, A_i is the peak of the total amount of unabsorbed gas in a single injection, T is the measured ambient temperature, and P is the actual atmospheric pressure.

$$D = \frac{\frac{V_{co}}{22.4} \times M \times 10^{-6}}{m \times w} \times 100\%$$

In the formula, m is the mass of the sample, the unit is g, w is the actual loading of Pt in the catalyst, and M is the molar mass of Pt (195.08 g mol^{-1}).

X-ray photoelectron spectroscopy (XPS) measurements were performed on a Thermo Scientific K-Alpha+ spectrometer with Al Kα excitation (1486.6 eV). The binding energy was calibrated using the C 1 s peak of surface adventitious carbon at 284.8 eV, and XPS Peak 4.1 software was used for peak fitting and quantitative analysis with a fitting error <0.1 eV.

Catalyst activity testing

In the laboratory, the catalyst performance was evaluated using a custom-built activity evaluation setup. A MultiGas 2030 Fourier Transform Infrared (FT-IR) gas analyzer was utilized to monitor gas concentrations in real-time. A 2 milliliter sample of 40–60 mesh catalyst was positioned within a quartz tube coated with quartz wool. A gas mixture, delivered at a total flow rate of 2.5 liters per minute, was composed of 500 ppm NO (nitric oxide), 500 ppm CO (carbon monoxide), 200 ppm C_3H_6 (propene), 100 ppm C_3H_8 (propane), 8% O_2, and 10% water vapor, balanced with N_2 (nitrogen). The space velocity was set at 80 000 milliliters per hour per liter of catalyst. Once the gas concentrations had reached equilibrium, the temperature was raised to 500 °C at a heating rate of 10 °C per minute. Data regarding reaction temperature and gas concentrations were collected throughout the heating process. The experiment was conducted twice, and the results from the second run were considered as the actual conversion rate of the catalyst.

For the performance evaluation of NO conversion, we use the proportion of NO_2 as an indicator. The specific calculation method is as follows:

$$X = \frac{C_{NO_2}}{C_{NO_X}}$$

Among them, C_{NO_2} represents the amount or concentration of NO_2 generated. And C_{NO_x} represents the total amount or concentration of nitrogen oxides (NO, NO_2, N_2O).

The formula for calculating the conversion of carbon monoxide, propene, propane is as follows:

$$Y = \frac{C_{in} - C_{out}}{C_{in}}$$

In the formula, C_{in} is the inlet reactant concentration and C_{out} is the outlet reactant concentration.

NO temperature-programmed desorption and *in situ* infrared spectroscopy

In situ diffuse reflection infrared Fourier transform spectra of NO(NO-DRIFTS) on catalysts were obtained using a Thermofisher Nicolet iS50 FT-IR spectrometer equipped with a photoconductivity detector (MCT), with a spectral resolution of 4 cm^{-1} and a scanning wavenumber range of 650–4000 cm^{-1}. A 100 milligram pretreated sample was placed in an *in situ* cell and pretreated in a nitrogen flow at 500 °C for 30 minutes, followed by cooling to 100 °C. From 100 °C to 400 °C, a background spectrum was recorded in a nitrogen flow at every 20 °C interval, and then the sample was cooled back to 100 °C. Each transient experiment was conducted in a gas stream of 8% O_2 + 500 ppm NO + 500 ppm CO, using the same measurement method as the background spectrum collection step. The total flow rate was 200 mL min^{-1}.

Result and discussion

Physicochemical properties of catalysts

Table 1 presents the physicochemical properties of the catalysts and their carriers. The Pt loading (measured by ICP-OES) varied slightly among the catalysts (1.01–1.02 wt%), which we attribute to differences in the solid content of the carriers. The aging samples show no obvious loss of Pt loading, indicating the good thermal stability of Pt species on the carriers. The specific surface areas of the synthesized catalysts decreased to varying degrees compared to the pure carriers—this is likely due to structural collapse caused by high-temperature calcination and pore clogging after Pt loading. However, Ce effectively anchored Pt atoms during synthesis, and La helped stabilize the catalyst's pore structure, which mitigated the reduction in specific surface area for Pt/LaAl-f and Pt/CeAl-f. Additionally, Ce and La promoted the formation of highly dispersed Pt on the catalyst surface, increasing the number of active Pt particles—a factor that is highly beneficial for catalytic reactions.

After aging, the specific surface area and Pt dispersion of all catalysts decreased significantly, which is a common phenomenon due to Pt particle aggregation and carrier sintering at high temperatures. Even so, the Ce- and La-modified samples showed better thermal stability, retaining more of their original surface structure compared to the unmodified Pt/Al catalyst. For example, Pt/LaAl-a retained a specific surface area of 94.31 m^2 g^{-1} (only a 6.3% loss from Pt/LaAl-f), whereas Pt/Al-a lost 22.5% of its specific surface area (from 103.56 m^2 g^{-1} to 80.23 m^2 g^{-1}). In terms of Pt dispersion, Pt/LaAl-f had a dispersion of 50.48%—more than twice that of Pt/Al-f (24.72%)—and after aging, Pt/LaAl-a still maintained a higher dispersion (40.70%) than Pt/Al-a (15.27%). The superior thermal stability of Pt/LaAl is closely related to the structural modification of γ-Al_2O_3 by La and the formation of $Al_{11}La_3$ intermetallic compounds, the existence and structural characteristics of which are systematically verified in the following section.

Fig. 1 presents representative TEM images and Pt particle size distribution histograms of fresh and aged catalysts. For fresh catalysts, the average Pt particle size follows the order: Pt/

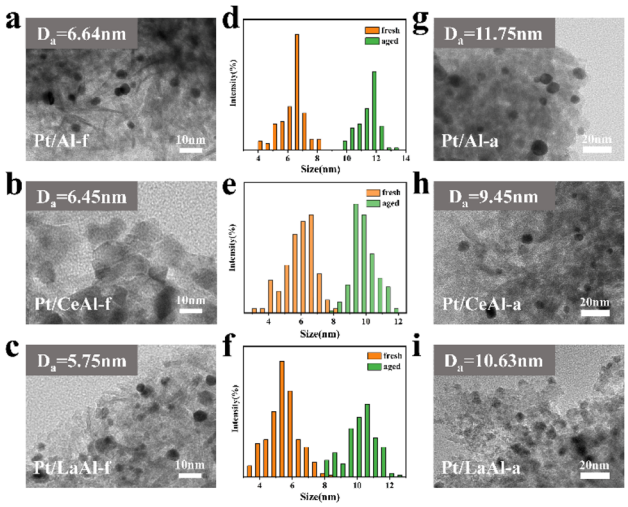

Fig. 1 (a–c, g and h) Representative TEM images of Pt loaded in different supports of (a) Pt/Al-f, (b) Pt/CeAl-f, (c) Pt/LaAl-f and after aging of (g) Pt/Al-a, (h) Pt/CeAl-a, (i) Pt/LaAl-a. (d–f) Particle size distribution histograms of Pt NPs on different supports.

Table 1 Physical properties of three Catalysts

Sample	Pt loading[a] (wt%)	S_{BET}[b] (m^2 g^{-1})	Pt dispersion[c] (%)	D_a[d] (nm)
γ-Al_2O_3	—	120.75	—	—
Pt/Al-f	1.01	103.56	24.72	6.64
Pt/Al-a	1.01	80.23	15.27	11.75
Ce-Al_2O_3	—	90.79	—	—
Pt/CeAl-f	1.02	88.69	49.01	6.45
Pt/CeAl-a	1.02	81.36	41.19	9.45
La-Al_2O_3	—	110.65	—	—
Pt/LaAl-f	1.01	101.98	50.48	5.75
Pt/LaAl-a	1.01	94.31	40.70	10.6

[a] ICP-OES test results. [b] Obtained by BET specific surface area assay. [c] Determined by CO pulse chemisorption test. [d] The average particle size of platinum on the catalyst was determined by TEM.

LaAl-f (5.75 nm) < Pt/CeAl-f (6.45 nm) < Pt/Al-f (6.64 nm). This trend aligns with the CO pulse chemisorption results (Table 1), where Pt/LaAl-f exhibits the highest Pt dispersion (50.48%). The smaller Pt particle size and higher dispersion in La/Ce-modified catalysts indicate that La and Ce can effectively inhibit Pt agglomeration during the synthesis process—likely due to strong interactions between the rare earth elements and Pt atoms, which anchor Pt nanoparticles on the carrier surface.

After aging at 750 °C for 10 hours, all catalysts show increased Pt particle sizes due to Oswald ripening (a common phenomenon where small nanoparticles dissolve and redeposit on larger ones at high temperatures). However, the degree of particle growth differs significantly: Pt/Al-a undergoes the most severe agglomeration, with its average Pt particle size increasing to 11.75 nm (a 77% increase from the fresh state). In contrast, Pt/LaAl-a and Pt/CeAl-a show more moderate growth, with average particle sizes of 10.63 nm (85% increase) and 9.45 nm (47% increase), respectively. This indicates that La and Ce modifications enhance the thermal stability of Pt nanoparticles, reducing their tendency to aggregate under harsh aging conditions. The retained small Pt particle size in aged Pt/LaAl-a and Pt/CeAl-a provides a structural basis for their superior catalytic activity compared to Pt/Al-a.

Characterization and verification of $Al_{11}La_3$ intermetallic phase

Fig. 2 shows the XRD patterns of fresh and aged Pt catalysts supported on the three carriers, with the partial magnification of 2θ in 25–35° for identifying $Al_{11}La_3$ and CeO_2 phases presented in the inset. The intense diffraction peak of γ-Al_2O_3 coincides with the characteristic diffraction peak of Pt (111) at approximately 39.7°, which obscures direct confirmation of Pt loading *via* XRD for fresh catalysts. However, after aging, the diffraction peak at 39.7° becomes significantly sharpened for all samples—particularly for Pt/Al-a—indicating the aggregation of Pt nanoparticles during high-temperature aging.

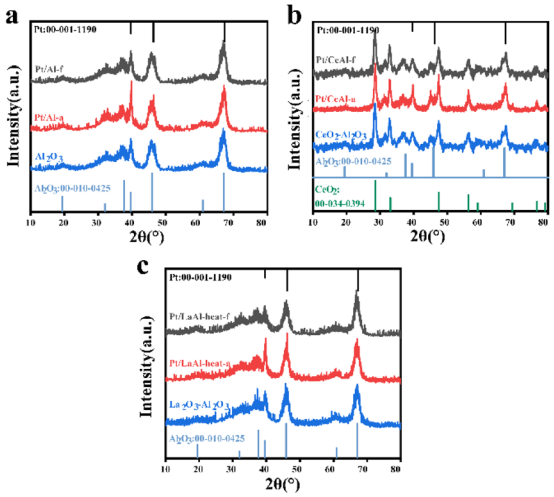

Fig. 2 XRD patterns of Pt-supported catalysts on different carriers.: (a) Pt/Al, (b) Pt/CeAl, (c) Pt/LaAl.

In the 2θ range of 30–40°, the characteristic diffraction peak of γ-Al_2O_3 exhibits distinct variations for Ce- and La-modified catalysts, reflecting the different occurrence forms of the two dopants. For Pt/CeAl, a well-resolved diffraction peak of CeO_2 is clearly detected at ~28.5° (JCPDS no. 34-0394), while the γ-Al_2O_3 peak shows the minimal broadening among all samples, confirming that Ce exists as a well-crystallized CeO_2 phase on the γ-Al_2O_3 surface rather than entering the carrier lattice. In contrast, no characteristic diffraction peaks of individual La oxides (*e.g.*, La_2O_3, LaOOH) are observed for Pt/LaAl, even though La is successfully doped into the catalyst system (verified by ICP-OES). Instead, the γ-Al_2O_3 characteristic peak of Pt/LaAl presents a distinct low-angle shift and significant peak broadening compared with Pt/Al and Pt/CeAl, which is a typical structural feature of lattice doping and lattice distortion caused by La^{3+} entering the γ-Al_2O_3 lattice.

Weak but distinct diffraction signals corresponding to $Al_{11}La_3$ intermetallic compound (PDF#00-024-0501) are detected at ~27.3° and ~32.6° for Pt/LaAl (Fig. 1c inset). The absence of independent La oxide peaks is mainly due to the low doping amount of La and its unique occurrence form: La^{3+} partially enters the γ-Al_2O_3 lattice to form a lattice-substituted solid solution (caused by the moderate ionic radius difference between La^{3+} (0.1032 nm) and Al^{3+} (0.0535 nm)), while the remaining La combines with Al to form low-crystallinity $Al_{11}La_3$ with small grain sizes. The low crystallinity and weak XRD signal of $Al_{11}La_3$ (masked by the strong γ-Al_2O_3 signal) result in no independent La-related diffraction peaks, but the lattice doping and distortion induced by La modification directly confirm the interaction between La and Al atoms, laying the foundation for the formation of $Al_{11}La_3$ phase.

To further confirm the existence of $Al_{11}La_3$ phase and its distribution on the carrier, EDS elemental mapping and SAED tests were performed on Pt/LaAl catalyst, with the results shown in figure. EDS elemental mapping results reveal that La elements are uniformly dispersed on the γ-Al_2O_3 carrier surface without obvious agglomeration , which excludes the formation of large La oxide particles and supports the uniform incorporation of La into the carrier matrix to form Al-La composite phases. SAED tests were conducted at different random positions of the Pt/LaAl catalyst to avoid accidental results, and the obtained diffraction ring patterns and lattice fringe spacing (Fig. 3b–g) were well-matched with the standard crystal structure of $Al_{11}La_3$ (PDF#00-024-0501). The measured lattice parameters of the diffraction rings are consistent with the theoretical values of $Al_{11}La_3$, which directly and visually confirms the existence of $Al_{11}La_3$ intermetallic compound in the La-doped catalyst.

The formation of $Al_{11}La_3$ phase in Pt/LaAl catalyst is also supported by thermodynamic evidence from La-Al binary phase diagram analysis in previous literatures. Relevant studies[11] have clearly demonstrated that the $Al_{11}La_3$ phase is a thermodynamically stable phase in the La-Al binary system at temperatures above 600 °C, which is highly consistent with the calcination temperature (600 °C) of fresh catalysts and the aging temperature (750 °C) in this study. This thermodynamic stability ensures that $Al_{11}La_3$ phase does not decompose or transform

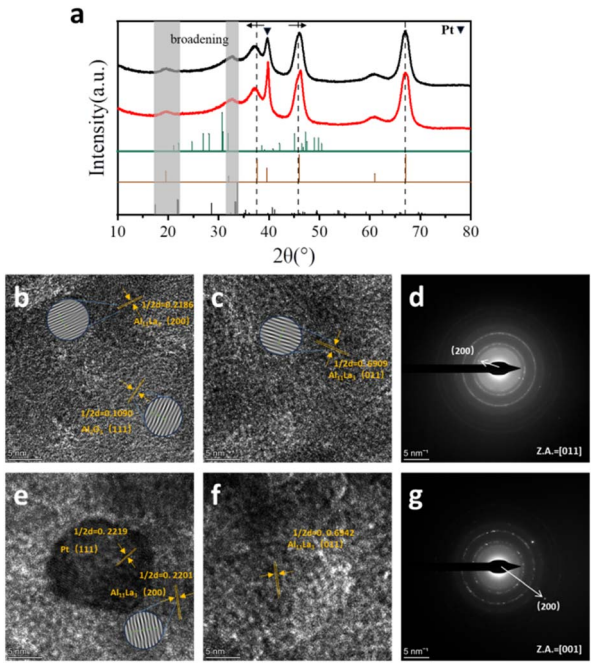

Fig. 3 Characterization of the existence of $AL_{11}LA_3$.

into other unstable phases during the high-temperature treatment process of the catalyst, thus providing a stable structural basis for the enhanced catalytic performance and aging resistance of Pt/LaAl.

In summary, the combined characterization results of XRD, EDS/SAED and thermodynamic evidence from literatures fully confirm the formation of $Al_{11}La_3$ intermetallic phase in Pt/LaAl catalyst. The uniform dispersion of La and the stable existence of $Al_{11}La_3$ phase not only modify the surface physicochemical properties of γ-Al_2O_3 carrier (*e.g.*, introducing additional Lewis acid sites and oxygen vacancies) but also strengthen the metal-carrier interaction with Pt, which is the core structural reason for the superior NO oxidation activity and aging resistance of Pt/LaAl catalyst.

NO oxidation activity of different catalysts

For fresh catalysts (Fig. 3a), the max NO_2 proportion follows the order: Pt/Al-f (79.2 ± 0.8%) > Pt/LaAl-f (78.7 ± 0.7%) > Pt/CeAl-f (75.7 ± 0.6%). However, a notable difference emerges in the low-temperature range (100–250 °C): Pt/LaAl-f exhibits a NO_2/NO_x of 48.5 ± 1.2% at 150 °C, which is 16.3% and 18.7% higher than that of Pt/Al-f (32.2 ± 0.9%) and Pt/CeAl-f (29.8 ± 0.8%), respectively. This superior low-temperature activity of Pt/LaAl-f is closely related to its smaller Pt particle size (5.75 nm) and higher Pt dispersion (50.48%)—smaller Pt nanoparticles provide more exposed active sites, and the enhanced metal-carrier interaction (discussed later) promotes the activation of NO molecules at low temperatures.

Correlating the activity results with catalyst physicochemical properties reveals two key relationships: (1) The max NO_2 proportion (at high temperatures, 350–400 °C) is positively correlated with the catalyst's specific surface area. Pt/Al-f has the largest specific surface area (103.56 m^2 g^{-1}) among fresh catalysts, which may provide more adsorption sites for reactant gases (NO and O_2), thereby achieving the highest max NO_2 proportion. (2) The proportion of low-temperature NO2 at 200 °C is negatively correlated with the average Pt particle size. Pt/LaAl-f, with the smallest Pt particle size, shows the best low-temperature activity, confirming that small Pt nanoparticles are critical for activating NO at low temperatures.

For aged catalysts (Fig. 3b), the activity order reverses to: Pt/LaAl-a (71.3 ± 0.8%) > Pt/CeAl-a (60.0 ± 0.7%) > Pt/Al-a (59.5 ± 0.6%). Pt/LaAl-a not only retains the highest NO_2 proportion but also maintains superior low-temperature activity. This retention of activity after aging is attributed to the stable structure of Pt/LaAl-a: it retains the largest specific surface area (94.31 m^2 g^{-1}) and smallest Pt particle size (10.63 nm) among aged catalysts, as well as the formation of $Al_{11}La_3$ intermetallic compounds (confirmed by XRD) that provide additional active sites.

Notably, while Pt particle size and specific surface area significantly influence activity, they are not the sole determinants. For example, Pt/CeAl-a has a smaller Pt particle size (9.45 nm) than Pt/LaAl-a (10.63 nm) but lower NO oxidation activity. This suggests that other factors—such as the chemical state of the catalyst surface and NO adsorption capacity—also play critical roles in governing catalytic performance.

Chemical analysis of NO oxidation reaction on catalysts

To explore the role of surface chemical states in NO oxidation, we analyzed the valence states of Pt and O on the catalyst surface using XPS.

Pt 4d XPS spectra. The Pt 4d orbital spectra (split into $4d_{5/2}$ and $4d_{3/2}$) were used to evaluate the valence state of Pt and metal-carrier interactions. For fresh catalysts, the binding energy of Pt $4d_{5/2}$ is ~314.2 eV for all samples—corresponding to metallic Pt (Pt^0), which is consistent with previous reports that Pt exists primarily in the metallic state in fresh Pt-supported catalysts. The proportion of Pt^0 (calculated *via* peak fitting) is similar across fresh samples (Pt/Al-f: 71.31%, Pt/CeAl-f: 72.74%, Pt/LaAl-f: 75.36%), indicating that the valence state of Pt is not the main factor causing activity differences among fresh catalysts.

After aging, the proportion of Pt^0 decreases for all samples (Pt/Al-a: 63.5%, Pt/CeAl-a: 60.64%, Pt/LaAl-a: 70.02%), likely due to partial oxidation of Pt by O_2 at high temperatures. However, the activity order of aged catalysts (Pt/LaAl-a > Pt/CeAl-a > Pt/Al-a) does not match the order of Pt^0 proportion, further confirming that Pt valence state is not the dominant factor governing NO oxidation activity.

A more significant observation is the shift in Pt 4d binding energy: Pt/LaAl shows a 0.8 eV shift to higher binding energy compared to Pt/Al, while Pt/CeAl shows a smaller shift of 0.4 eV. This binding energy shift is a direct indicator of enhanced metal-carrier interaction (SMSI): the electronegative La/Al or Ce/Al species in the modified carriers withdraw electron density from Pt atoms, increasing the binding energy of Pt orbitals. The stronger SMSI in Pt/LaAl not only inhibits Pt aggregation (as observed in TEM) but also modulates the adsorption strength of

NO molecules—promoting NO activation while preventing excessive adsorption that would block active sites.

O1s XPS spectra. The O1s spectra were deconvoluted into two peaks: (1) lattice oxygen (O lattice, ~529.8 eV), (2) oxygen vacancies (O_{vac}, ~532.0 eV). For fresh catalysts, the proportion of O_{vac} is low and similar across samples (Pt/Al-f: 32.03%, Pt/CeAl-f: 33.84%, Pt/LaAl-f: 32.09%), as the abundant surface hydroxyl groups (–OH) mask the signal of oxygen vacancies.

After aging, the surface hydroxyl groups are removed by high-temperature calcination, revealing a significant difference in O_{vac} proportion: Pt/LaAl-a has the highest O_{vac} proportion (34.39%), followed by Pt/CeAl-a (23.74%) and Pt/Al-a (23.45%). Oxygen vacancies are critical for NO oxidation because they act as adsorption sites for O_2 molecules—O_2 is adsorbed and activated at vacancies to form reactive oxygen species (*e.g.*, O_2^-, O^-), which then react with adsorbed NO to form NO_2. The high O_{vac} proportion in Pt/LaAl-a explains its superior NO oxidation activity: it provides more sites for O_2 activation, accelerating the reaction kinetics of NO oxidation.

To validate this hypothesis, NO temperature-programmed desorption (NO-TPD) was utilized to directly evaluate the catalysts' NO adsorption capabilities. The NO-TPD data revealed two desorption peaks: one at low temperatures (<300 °C) and another at elevated temperatures (300–500 °C). The NO adsorption capacity of the fresh catalysts was ordered as Pt/LaAl > Pt/CeAl > Pt/Al, with Pt/LaAl showing the highest performance. At 500 °C, the total NO desorption efficiency was ranked as Pt/Al-f > Pt/LaAl-f > Pt/CeAl-f. Pt/LaAl-f exhibited desorption peaks at 189 °C and 386 °C, respectively, with higher temperatures suggesting a stronger interaction with NO. Despite the decrease in NO adsorption capacity of aged samples, the overall desorption efficiency increased. The temperature shift in the low-temperature and high-temperature desorption zones suggests that aging results in the formation of more thermally stable intermediates, affecting the catalytic performance.

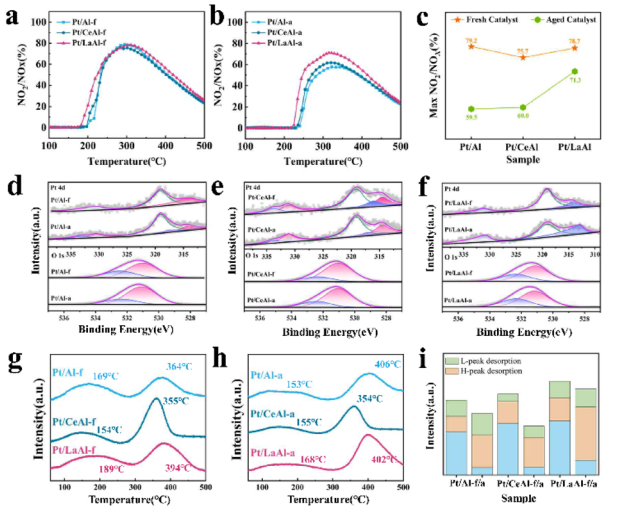

Fig. 4 (a–c) NO oxidation activity test chart, (d–f) catalyst XPS 4d spectrum, (g–i) catalyst NO-TPD test result graph.

To directly evaluate the NO adsorption capacity of catalysts, we conducted NO-TPD experiments (Fig. 4). All catalysts exhibit two desorption peaks: a low-temperature peak (*L*-peak, <300 °C) corresponding to weakly adsorbed NO and a high-temperature peak (*H*-peak, 300–500 °C) corresponding to strongly adsorbed NO.

For fresh catalysts, the total NO desorption amount (integral of *L*-peak + *H*-peak) follows the order: Pt/LaAl-f > Pt/CeAl-f > Pt/Al-f. Pt/LaAl-f also shows a higher H-peak temperature (386 °C) than Pt/Al-f (325 °C) and Pt/CeAl-f (348 °C), indicating stronger adsorption of NO on Pt/LaAl-f—consistent with the enhanced SMSI observed in XPS. The strong NO adsorption on Pt/LaAl-f promotes NO activation, while the high total adsorption capacity ensures sufficient reactant supply for the reaction.

After aging, the total NO desorption amount decreases for all samples , but the order remains unchanged. Notably, the H-peak temperature shifts to higher values (Pt/LaAl-a: 402 °C, Pt/CeAl-a: 375 °C, Pt/Al-a: 351 °C), suggesting that aging increases the strength of NO adsorption—likely due to the formation of more stable NO-catalyst surface complexes. This enhanced adsorption strength, combined with the retained high adsorption capacity, contributes to the superior activity of aged Pt/LaAl-a.

In situ infrared spectroscopy analysis

In situ DRIFTS was used to identify the intermediate species formed during NO adsorption and oxidation, providing insights into the reaction mechanism (Fig. 5).

NO adsorption at 60 °C. After saturated NO adsorption at 60 °C, the DRIFTS spectra of the three catalysts show distinct intermediate species:

Pt/Al: Five characteristic peaks are observed: 1615 cm^{-1} (NO_2 interacting with –OH groups), 1586 cm^{-1} (bridged bidentate nitrate), 1560 cm^{-1} (monodentate nitrate), 1300 cm^{-1} (bridged bidentate nitrite), and 1257 cm^{-1} (bridged bidentate nitrite). The weak intensity of these peaks indicates low NO adsorption capacity—consistent with NO-TPD results.[12–14]

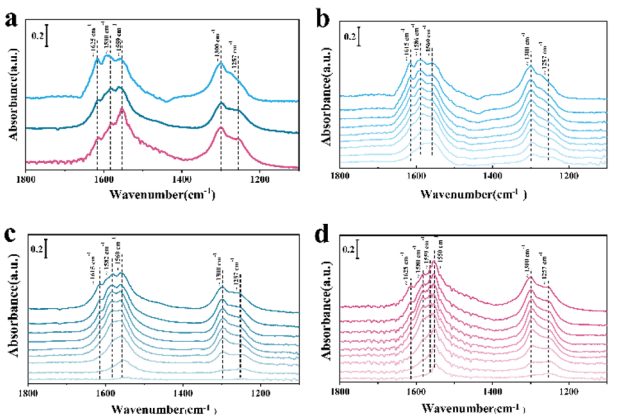

Fig. 5 *In situ* Fourier transform infrared spectroscopy of platinum catalysts loaded on different carriers: (a) saturated adsorption and programmed temperature desorption (b) Pt/Al, (c) Pt/CeAl, (d) Pt/LaAl.

Pt/CeAl: Similar peaks are observed, but the 1615 cm^{-1} peak (weakly adsorbed NO_2) is significantly weaker than that of Pt/Al. This suggests that Pt/CeAl has a lower ability to adsorb NO_2, which may reduce the coverage of NO_2 on active sites but also indicates insufficient activation of NO to form stable nitrate intermediates.

Pt/LaAl: The spectra show stronger peaks for nitrate species: 1580 cm^{-1} (bridged bidentate nitrate), 1559 cm^{-1} (chelating bidentate nitrate), and 1550 cm^{-1} (monodentate nitrate). The intensity of these peaks is 1.8–2.2 times higher than that of Pt/Al, confirming the higher NO adsorption capacity of Pt/LaAl. Additionally, the 1625 cm^{-1} peak (weakly adsorbed NO_2) is weak, indicating that most NO is converted to stable nitrate intermediates rather than weakly adsorbed NO_2—this is critical for efficient NO oxidation, as stable nitrates can further react with O_2 to form NO_2.

The abundance of bridging/chelating nitrate species on Pt/LaAl is attributed to the formation of $Al_{11}La_3$ intermetallic compounds: these compounds introduce new Lewis acid sites on the carrier surface, which strongly adsorb NO_x species and stabilize nitrate intermediates. This explains why Pt/LaAl exhibits higher NO adsorption capacity and superior catalytic activity.

Temperature-programmed desorption of intermediates. When the temperature is increased from 100 °C to 500 °C, the evolution of intermediate species differs among catalysts:

Pt/Al: The weakly adsorbed NO_2 peak (1630 cm^{-1}) disappears at 150 °C, followed by a gradual decrease in nitrate peaks (1602 cm^{-1}, 1569 cm^{-1}) between 200–350 °C. The nitrite peaks (1302 cm^{-1}, 1260 cm^{-1}) start to decrease at 300 °C and disappear at 450 °C. This indicates that nitrate is the main active intermediate (consistent with the *L*-peak in NO-TPD), while nitrite is a secondary intermediate that is converted to nitrate before desorption.

Pt/CeAl: The evolution trend is similar to Pt/Al, but the intermediate peaks disappear earlier (nitrate peaks vanish at 400 °C, nitrite at 420 °C). At 500 °C, almost no intermediate species remain on Pt/CeAl, indicating poor NO storage capacity—consistent with the low NO desorption amount in NO-TPD.

Pt/LaAl: The nitrate peaks (1610 cm^{-1}, 1580 cm^{-1}, 1550 cm^{-1}) persist until 450 °C, and the nitrite peaks are converted to nitrate between 300–350 °C (showing a temporary increase in nitrate intensity). At 500 °C, weak nitrate signals still remain, indicating that Pt/LaAl not only has high NO adsorption capacity but also retains intermediates at higher temperatures—providing a continuous supply of reactants for NO oxidation.

Based on these results, we propose a reaction mechanism for NO oxidation on Pt/LaAl: (1) NO is adsorbed on Pt active sites and oxygen vacancies to form adsorbed NO species; (2) O_2 is activated at oxygen vacancies to form reactive oxygen species; (3) adsorbed NO reacts with reactive oxygen to form nitrate/nitrite intermediates; (4) nitrate intermediates decompose or react further to form NO_2, which desorbs from the catalyst surface. The formation of $Al_{11}La_3$ intermetallic compounds enhances NO adsorption and intermediate stability, while the strong SMSI inhibits Pt aggregation—together, these factors contribute to the superior performance of Pt/LaAl.

Conclusions

This study investigates the performance of Pt-supported catalysts on γ-Al_2O_3, Ce-doped γ-Al_2O_3 (Ce-Al_2O_3), and La-doped γ-Al_2O_3 (La-Al_2O_3) for NO oxidation in diesel exhaust aftertreatment, focusing on the effect of carrier modification. Results show that La- and Ce-doped carriers significantly enhance the thermal stability of Pt catalysts: after aging at 750 °C for 10 h, Pt/LaAl-a retains a specific surface area of 94.31 $m^2\ g^{-1}$ (only a 6.3% loss) and Pt dispersion of 40.70%, outperforming unmodified Pt/Al-a which suffers a 22.5% surface area loss and retains just 15.27% Pt dispersion. La modification is particularly impactful as it promotes the formation of $Al_{11}La_3$ intermetallic compounds in Pt/LaAl, which provide additional NO adsorption sites and stabilize active nitrate intermediates—Pt/LaAl-f exhibits a NO adsorption capacity of 89.6 μmol g^{-1} (nearly twice that of Pt/Al-f's 45.1 μmol g^{-1}) and maintains superior low-temperature activity (38.5% NO_2 proportion at 200 °C for fresh samples and 31.2% at 250 °C for aged samples). Correlation analysis confirms that NO oxidation activity is more strongly governed by NO adsorption capacity than by Pt particle size or valence state, with Pt/LaAl's high adsorption capacity ensuring sufficient reactant supply and stable intermediates. Additionally, La strengthens the metal-carrier interaction (SMSI) between Pt and the carrier (evidenced by a 0.8 eV shift in Pt 4d binding energy), suppressing Pt aggregation (Pt/LaAl-a has an average Pt particle size of 10.63 nm *vs.* 11.75 nm for Pt/Al-a) and balancing NO adsorption and activation. Overall, La-doped γ-Al_2O_3 emerges as a promising carrier for Pt-based diesel oxidation catalysts (DOC), and the insight that regulating NO adsorption capacity *via* intermetallic compounds and SMSI is the primary driver of enhanced NO oxidation activity provides valuable guidance for designing durable, high-efficiency catalysts for diesel exhaust and industrial NO_x purification.

Conflicts of interest

There are no conflicts to declare.

Data availability

The data that support the findings of this study are available from the corresponding author upon reasonable request.

Supplementary information (SI) is available. See DOI: https://doi.org/10.1039/d6ra00070c.

Acknowledgements

This work was financially supported by the Science and Technology Talent and Platform Program (Grant Nos. 202305AF150109, 202305AD160018) and the Project of Yunnan Precious Metals Laboratory (Grant No. YPML-2023050203). The authors also acknowledge the technical support from the State Key Laboratory of Precious Metal Functional Materials for providing characterization facilities.

Notes and references

1 S. A. Yashnik, Z. R. Ismagilov, A. V. Porsin, *et al.*, *Top. Catal.*, 2007, **42–43**(1–4), 465–469.
2 Y. Ding, H. Yin, J. Wang and *et al.*, in. *Mobile Source Emission Regulations*, Springer, Singapore,2024.
3 A. Russell and W. S. Epling, *Catal. Rev.*, 2011, **53**(4), 337–423.
4 Y. Shi, Z. Li, J. Wang, *et al.*, *Appl. Catal. B Environ.*, 2021, **286**, 119936.
5 Y. Pu, X. Xie and W. Jiang, *Chin. Chem. Lett.*, 2020, **31**(10), 2549–2555.
6 N. Wei, C. Zhao, X. Hu, *et al.*, *Sci. Total Environ.*, 2023, **855**, 158881.
7 A. V. Karre, R. K. Garlapalli and A. Jena, *Catal. Commun.*, 2023, **179**, 106682.
8 E. Xue, K. Seshan and J. Ross, *Appl. Catal. B Environ.*, 1996, **11**(1), 65–79.
9 J. Jones, H. Xiong, A. T. DeLaRiva, *et al.*, *Science*, 2016, **353**(6295), 150–154.
10 S. Xie, W. Tan, C. Wang, *et al.*, *J. Catal.*, 2022, **405**, 236–248.
11 K. A. Gschneidner and F. W. Calderwood, *Bull. Alloy Phase Diagr.*, 1988, **9**(6), 686–689.
12 T. Liu, L. Wei, Y. Yao, *et al.*, *Appl. Surf. Sci.*, 2021, **546**, 148971.
13 Y. Ji, S. Bai and M. Crocker, *Appl. Catal. B Environ.*, 2015, **170–171**, 283–292.
14 F. Prinetto, M. Manzoli, S. Morandi, *et al.*, *J. Phys. Chem. C*, 2010, **114**(2), 1127–1138.